Size and Shape Dependent Photocatalytic Activity of Au and Pt Deposited-Zinc Sulfide Nanocomposites

A

Thesis submitted

In partial fulfillment of the requirement for the degree of

Master of Science

In

Chemistry

Submitted by

Shilpa Singla

(Reg. No. 300902018)

Under the supervision of

Dr. Bonamali Pal

Assistant Professor

School of Chemistry & Biochemistry

Thapar University

Patiala 147001

Punjab

June 2011

Contents

1. Introduction

1.1 Principle of photocatalysis

Photocatalysis consists of the combination of photochemistry and catalysis. It implies that light and a catalyst are necessary to generate or to accelerate a chemical reaction by generating positive holes (h^+) in the valence band (VB) and photoexcited electrons (e^-) in conduction band (CB) of semiconducting materials. Generation of these charge carriers (h^+ and e^-) occurs when a semiconductor is photoirradiated with energy, *hν* equal to or greater than the band gap energy, *Eg*. The photoexcited electron and positive hole undergo relaxation to the bottom of the CB and top of the VB, respectively, and induce reduction and oxidation of the chemical substances adsorbed on the surface of the photocatalyst [1-5]. The holes either oxidize the water (Eqn 1) or hydroxyl ions (Eqn 2) or react directly with organic compounds (Eqn 3) and the electrons can be accepted by the oxygen present in solution to form superoxide ion (Eqn 4) or in a reaction together with oxygen and H^+ to form hydrogen peroxide (Eqn 5) which ultimately dissociates to hydroxyl radicals and hydroxyl ions (Eqn 6) as shown below.

$$ZnS + h\nu \rightarrow h^+ + e^-$$

$$h^+ + H_2O\,(ads) \rightarrow {\bullet}OH + H^+ \quad (1)$$

$$h^+ + OH^-\,(ads) \rightarrow {\bullet}OH \quad (2)$$

$$h^+ + RH\,(ads) \rightarrow {\bullet}R + H^+ \quad (3)$$

$$e^- + O_2\,(ads) \rightarrow O_2^- \quad (4)$$

$$2e^- + O_2\,(ads) + 2H^+ \rightarrow H_2O_2 \quad (5)$$

$$e^- + H_2O_2\,(ads) \rightarrow {\bullet}OH + OH^- \quad (6)$$

All of these produced species are highly oxidizing and reactive, capable of attacking and breaking down the organic compounds that come in contact with the photocatalyst surface. This oxidation and reduction ability of the photoexcited electron and hole is highly dependent on the energetics of CB and VB position, oxidation and reduction potentials of the substrate and surface morphology of photocatalyst. Hence the photoactivity of desired material can be tuned by changing the size & shape which in-turn alter the redox ability of CB and VB. Moreover, there is a possibility of recombination of CB-electron – VB-hole pair which dissipates as heat. This recombination can be avoided by noble metal deposition because the photogenerated electrons are quickly transferred to conducting metal islands and prevent the recombination of

photoexcited electron-hole pair and thereby improves the photooxidation of the adsorbed substrate by strongly reactive holes.

1.2 Effect of metal photodeposition

Contact of the metal with the semiconductor influences the energetics and the interfacial charge transfer processes within the metal-photocatalyst particle [6, 7]. When a metal like Ag/Fe/Au/Pt get attached to the surface of the photocatalyst, the Fermi energy level (which is size and shape dependent) of both come to equilibrium [8]. The metal picks up the photoexcited CB electron that diffuses to the surface of photocatalyst before their recombination with VB holes [9, 10]. In the process, metal ions are reduced to elemental metal and thereby, the metal deposits act as a sink of electrons. On the other hand, the hole accepts electrons from the electron rich species like methanol and gets oxidized to HCHO and H_2 (Scheme 1).

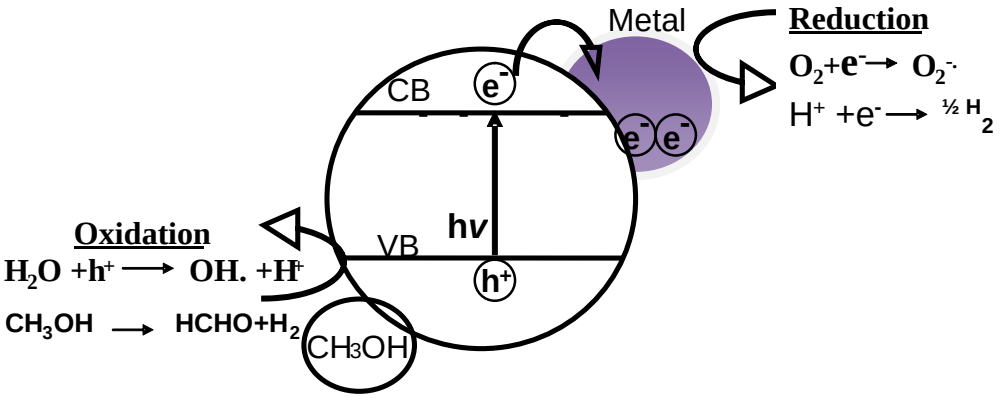

Scheme 1. Effects of metal, Au, Ag, Pt, Fe etc (electron acceptor) and CH_3OH (electron donor) on ZnS nanoparticles.

Choice of metal is done on the basis of their reduction potential. Metals which have lower reduction potential than semiconductor photocatalyst are preferred, as more and more electrons get transfer to the metal and further to the reacting species. This fact prevents the recombination and thereby improves the photoactivity, the extent being dependent on electron affinity, charge transfer ability, interface area, Fermi energy, and particle size & shape of the deposited metals. The VB holes are powerful oxidants (+1.0 to +3.5 V vs NHE depending on the semiconductor and pH), while the conduction-band electrons are good reductants (+0.5 to -1.5 V vs NHE). The efficiency of a semiconductor can be further increased by changing its size and shape. On bulk (large size) semiconductor particles, only one species, either the hole or electron, is available for reaction due to band bending. However, in very small semiconductor particle suspensions both species are present on the surface.

1.3 Effect of size and shape of semiconductor particles

The fate of photoelectrochemical reactions and optoelectronic properties of semiconductor materials are drastically changed with size and shape of the catalysts particles [11-22]. As the size of particles is reduced to below 10-20 nm, called as quantum size particles their reductive/oxidative ability increases. With the decrease in size of particles, the percentage of surface active atoms increases and the surface to volume (S/V) ratio drastically increases [12]. The surface atoms are chemically more active compared to the bulk atoms because they usually have fewer adjacent coordinate atoms and unsaturated sites. Due to this high S/V ratio of smaller particles, and due to shift in band edge position, the photoexcited charge carriers are diffused to reach the surface quickly and react instantaneously with the adsorbed species on the photocatalyst surface. For very small particles no internal electric held is necessary to separate photogenerated electron-hole pairs. Therefore, possibility for the charge carriers to reach the interface increased, as the size of particles decreased. Moreover, when particle's shape changes from spherical to rod, hollow tube, hexagonal and other geometrical shape, the reactivity of these materials is abruptly changed due to improved charge transfer process. Compared to nanospheres (NS), nanorods (NR) of both metal and semiconductor have become popular choice due to higher photon absorption cross sections, enhanced photovoltaic efficiencies**,** size-dependent, controlled aspect ratio, and polarized light absorption scattering & emission [17].

1.4 Types of semiconductors and their influence on photocatalytic processes

The extent of desired photoreduction and photooxidation of a chemical reaction induced by photocatalyst largely depends on its band edge position of the CB and VB [4, 23-25]. In an ideal system, conduction band level should be well above (more negative than) the hydrogen or any other reduction potential level of the substrate to be reduced and valence band edge should be well below (more positive than) the water or any other oxidation potential level of the substrate for an efficient production of hydrogen and oxygen from water by photolysis (Figure 1).

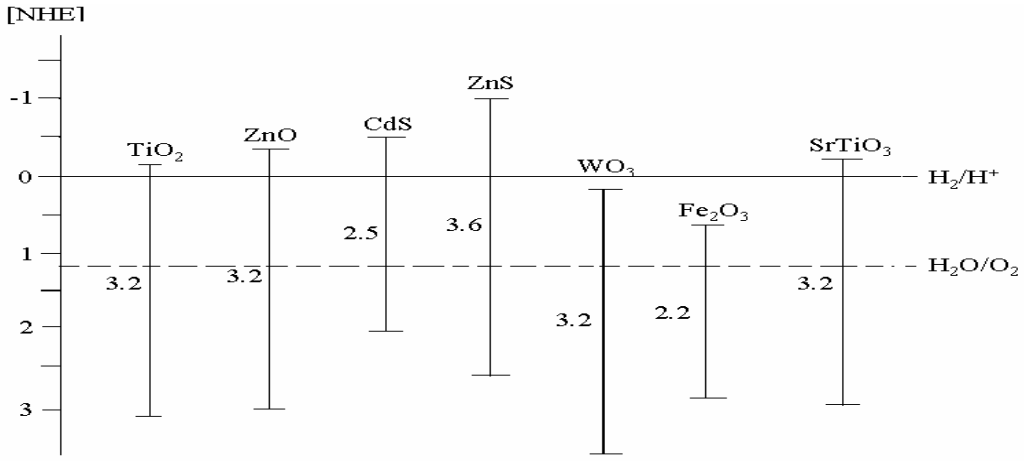

Figure 1. Comparisons of band gap of different semiconductors.

It is evident from the Figure 1 that the ease of H^+ reduction to H_2 e.g., ½ H^+ → H_2, is found to decrease gradually in the order ZnS> CdS> ZnO> $SrTiO_3$> TiO_2 owing to decreasing CB edge position towards less negative direction. Thus, by judicious selection of photocatalysts, depending upon the relative positions of valence and conduction band edge, semiconductors can be used to carry out photochemical redox reactions dependent on the nature and amount of metal/catalysts, light intensity and the band gap energy. Some of the semiconductors satisfying both the above conditions are TiO_2, WO_3, ZnO, ZnS and CdS etc. It can be seen that ZnS has high negative value of CB band position/potential as compared to other photocatalysts which may favour the photocatalytic reduction reaction in higher extent than any other semiconductors as mentioned in figure 1. ZnS is a direct wide band gap (for the bulk cubic and hexagonal phases of ZnS, Eg = 3.68 and 3.80 eV, respectively) semiconductor. ZnS crystal usually exhibits a polymorphism of two phases with different stacking sequences of close packed planes to each structure: one is the cubic phase with a zinc blende structure (c-ZnS); and the other is the hexagonal phase with a wurtzite structure (h-ZnS) [26]. ZnS shows remarkable chemical stability against oxidation and hydrolysis. These properties are retained when the particle size steps down to 10 nm and below, and thus ZnS nanoparticles are interesting entities for optical and catalytic functions. Moreover, ZnS may be doped by a host of elements, so that the electrical and optical properties can be tuned over an extended range [27]. The most widely used photocatalyst, TiO_2 is an indirect band-gap semiconductor, and thus the generation efficiency of photoexcited charge carrier is low. However, ZnS is a direct band-gap semiconductor; hence the generation efficiency of photogenerated charge carrier is higher. The above statements show the potential of ZnS as an important semiconductor in various applications, especially in reductive photocatalytic reactions. However, ZnS has not been potentially used because of its low surface activity.

2. Literature review

Extensive research is currently going on regarding synthesis and applications of various metal and semiconductors nanospheres, nanorods, nanowires, nanosheets etc. because altering the shape and size of the particle, alters the degree of confinement of the electrons, and affects the electronic structure of the solid. There are several reports regarding the synthesis of ZnS nanostructures of different sizes and shapes. Hua-Feng et al. synthesized ZnS hollow nanospheres with nanoporous shell through the evolvement of ZnO nanospheres which were synthesized by hydrothermal method with poly (sodium-p-styrene sulfonate) (PSS) as surfactant at low temperature [28]. The controllable synthesis of ZnS nanocrystals with desirable morphology and correlative structure has been carried out via the solvothermal method by simply changing the molar ratio of the reactants. Zepeng Li et al. synthesized hexagonal-shaped ZnS nanosheets with a zinc-blende structure and ZnS nanorods with wurtzite structure. The photoluminescence spectra of the ZnS nanosheets and nanorods exhibit different emission bands. ZnS nanosheets show a strong emission at 534 nm while the nanorods have two emissions located at 520 and 578 nm [29]. Chun Lan et al. fabricated ZnS nanorods by annealing precursor ZnS nanoparticles, which were prepared by one-step, solid-state reaction of $ZnCl_2$ and Na_2S through grinding by hand at ambient temperature, in NaCl flux [30]. Some researchers have demonstrated the formation of wurtzite ZnS nanoplates in a medium of CS_2, benzene, pyridine, or absolute ethanol by a mild solvothermal process over a temperature from 160 to 200 °C [31].

Visible light sensitive Cu-doped ZnS hollow photocatalyst particles; “Cu-ZnS-shell” could generate H_2 through photocatalytic decomposition of HS^- ion in Na_2S solution. The photoactivity under xenon lamp irradiation was 6 and 130 times higher than that of copper-free “ZnS-shell” and co-precipitated ZnS particles, respectively [32]. Kakuta et al. investigated the hydrogen

production in aqueous sulfite solution using ZnS and CdS co-precipitated into Nafion films. An efficient hydrogen production (quantum yield of 0.90) can be achieved by irradiating suspensions of ZnS in various electrolyte solutions and the rate of this reaction strongly depends on the quality of the ZnS photocatalyst. Primary amines can be converted to secondary amines via two-electron photoreduction of the Schiff bases formed photooxidatively on illuminated ZnS. Geometric and valence isomerisation of unsaturated organic molecules occur on illuminated photocatalysts for the cis-trans isomerisation of several simple alkenes proceeds with a light conversion efficiency greater than unity on suspended particles of ZnS, & CdS.

Ranjit et al. tested the photocatalytic reduction of nitrite and nitrate to ammonia on ZnS [33]. Some researchers found that ZnS nanocrystallites prepared in N,N-dimethylformamide (DMF) photocatalyze dehalogenation of halogenated benzenes to benzene as the final product from chlorinated benzenes and to difluorobenzenes from fluorinated benzenes in the presence of triethylamine (TEA) as an electron donor under UV light irradiation (λ> 300 nm) [34]. Yanagida et al. showed that the ZnS suspension prepared by cooling from aqueous $ZnSO_4$ and Na_2S solutions catalyzes photoredox reactions of acetaldehyde, giving ethanol without much H_2 evolution as a two-electron- reduction product, and acetic acid, biacetyl, and acetoin as oxidation products [35]. The $ZnS/Zn_3(PO_4)_2$ $.4H_2O$ heterostructured hemispheres showed strongly structure-induced enhancement of photocatalytic performance for the photodegradation of Rhodamine [36]. Photocatalytic reduction of aromatic azides to amines using CdS and CdSe nanoparticles have been found to very efficient and highly chemoselective. The parameters affecting the product yields are (i) the reducing power of the photoexcited semiconductor which follows the order CdS> TiO_2> WO_3 where activity of ZnS is not known and (ii) nature & amount of various metal loading which are important factors that is lacking during photocatalytic organic synthesis and still need to be investigated cautiously.

From the current research as mentioned above it is found that that most of the work has been carried out regarding the synthesis of ZnS nanostructures of different shapes and sizes. Mainly structural characterization, optical absorption & fluorescence emission were studied. Size and shape dependent photoreactivity and optoelectronic property of nanocatalysts like TiO_2, ZnO, CdS have been studied for enhancing their performance in practical uses. However, ZnS has not been studied extensively in this direction and there are few reports about the comparative photoactivity of ZnS nanosphere and nanorod morphology and the effect of metal loading. Also information about the reductive photoactivity of ZnS in comparison to other highly active photocatalysts is lacking. Although extensive research has done for H_2 photogeneration using ZnS, its reductive ability in organic functional group transformation and oxidative degradation of toxic compounds has not been explored much.

3. Objectives

(I) Synthesis of ZnS nanosphere & nanorod and photodeposition of gold and platinum to make metal-ZnS nanocomposites.

(II) Investigation of shape dependent optical properties such as absorption and emission and other characterization (HRTEM/SEM/XRD) for determining size and shape of the as-synthesized nanoparticles.

(III) Investigation of photocatalytic efficiency of ZnS nanoparticles by reaction with various substrates and to show the effect of variation of shape and metal loading on the rate of photochemical reaction.

4. Experimental Work

4.1 Materials used

All the reagents used were of analytical grade or of highest purity. Zinc acetate ($Zn(CH_3COO)_2 \cdot 2H_2O$) (S D Fine Chem Limited), Sodium sulfide ($Na_2S.\ xH_2O$) (AR; Loba Chemie), NaOH (Extra pure; Loba Chemie), Thiourea (NH_2CSNH_2) (Loba Chemie), Ethylenediamine ($C_2H_4(NH_2)_2$) (S D Fine Chem Limited), Chloroauric acid ($HAuCl_4.\ xH_2O$) (Loba Chemie), Silver nitrate ($AgNO_3$) (Qualigens), and Chloroplatinic acid hydrate ($H_2PtCl_6.\ xH_2O$) (Sigma-Aldrich) were used as received without further purification.

4.2 Synthesis of ZnS nanostructures

ZnS nanospheres **:** ZnS nanospheres were successfully synthesized by reflux under an alkaline medium. An appropriate amount of zinc acetate (0.1 M), sodium sulfide (0.1 M), NaOH (5 M) and deionised water (100 mL) were refluxed together for 5 h under constant stirring. Upon reflux, the product was centrifuged and washed several times with deionised water. The sample was then dried in the oven at 80ºC for 2 h to obtain powder of ZnS nanospheres which appear white in colour [27].

ZnS nanorods **:** The synthesis of ZnS nanorods was carried out in a closed cylindrical teflon-lined stainless steel chamber of 80 mL capacity, using solvothermal technique. The schematic diagram of the chamber has been shown in Figure 2.

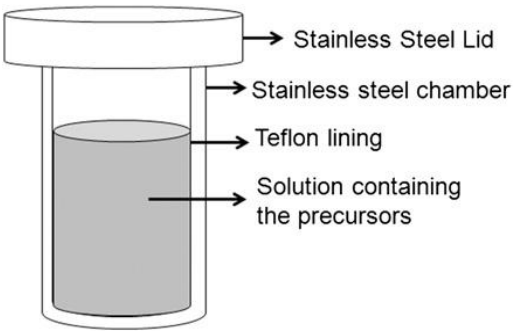

Figure 2. Schematic diagram of the teflon-lined stainless steel chamber used for the solvothermal synthesis of the nanostructures.

Thiourea was chosen as the sulphur source in the experiment because thiourea can dissolve and release S^{2-} ions in aqueous solution at elevated temperatures. Zinc acetate was employed as the zinc source. Zinc acetate and thiourea in the molar ratio of 1:3 were loaded into the teflon-lined chamber, which was filled to 80% of its total capacity with a mixture of ethylenediamine and deionised water in 1:1 volume ratio [29, 37-40]. After being fully stirred, the autoclave was sealed and put into an oven which was maintained at 200ºC for 12 h and then cooled to room temperature. The resulting precipitates were filtered off and washed repeatedly with deionised water and ethanol. The final products were dried in a vacuum at 80ºC for 6 h to obtain ZnS powder.

4.3 Metal loading on as-synthesised ZnS nanoparticles

The photoreactor consists of two glass tubes arranged concentrically, one having a larger diameter for water circulation and a smaller diameter tube is inserted in it which has a 125 W Hg arc lamp. In the present experimental section, the outer jacket of the reactor was removed and the samples were irradiated directly in test tubes surrounding the UV lamp. The test tubes were kept at a distance of 2-3 cm from the UV lamp and were placed on a magnetic stirrer. The whole assembly was kept in a wooden box to prevent the exposure from the UV light. A rough sketch of photoreactor is shown in Figure 3.

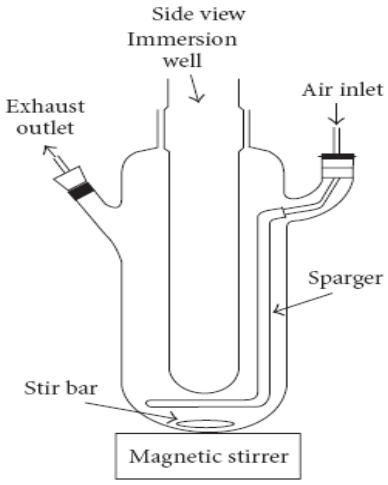

Figure 3. Photoreactor.

For metal photodeposition, 100 mg of ZnS sample was taken in a test tube. Then calculated amount of metal salt solution and 10 mL of 1:1 mixture of isopropanol and water was added to the test tube. For 1% gold deposition, 0.01M $HAuCl_4$ solution (507.6 µL) and for 1% platinum deposition, 0.01 M H_2PtCl_6 salt solution (512.82 µL) was taken. Nitrogen gas was purged from

this mixture for 15 min, after gas purging the test tube was sealed with parafilm so that there should be no air present in test tube and the inert atmosphere should remain as such, otherwise which can affect the metal deposition process. This solution was then UV irradiated for 2 hours under continuous stirring. Then this metal deposited solution was given subsequent washings, first with water (3 x 10 mL) and then with methanol (2 x 5 mL). After washing the wet solid material was taken in a petridish and dried in oven at 80ºC for 30 minutes. After drying, the solid sample was scratched from the petridish and sintered at 500ºC for 2 hours.

4.4 Photocatalytic test reactions

Photocatalytic degradation of p-nitrophenol (PNP)

For PNP degradation, 5 mL of 10 µM solution of PNP prepared in distilled water was added to the test tube containing 50 mg of ZnS nanorod (NR)/ or nanosphere (NS). This test solution was then irradiated in photoreactor for different time intervals, under continuous stirring. After irradiation for a definite time interval, the test solution was filtered using 0.22 µm cellulose filter to remove the catalyst. Then the test solution was analysed using UV-Vis spectrophotometer. The photocatalytic activity of ZnS-NR/NS, 1 wt% Au deposited ZnS-NR & NS and 1 wt% Pt deposited ZnS-NR & NS and the sintered samples were tested.

Photocatalytic oxidation of Benzaldehyde

For benzaldehyde oxidation, similar procedure was followed as was done in case of PNP degradation. 5mL of 10 µM benzaldehyde solution prepared in distilled water was added to the test tube containing 50 mg of ZnS nanostructures. This test solution was then irradiated in photoreactor for different time intervals, under continuous stirring. After irradiation for a definite time interval, the test solution was filtered using cellulose filter. Then the UV-Vis spectra of these solutions were taken.

Photocatalytic reduction of Benzaldehyde

For benzaldehyde reduction, 5 mL of 10 µM benzaldehyde solution prepared in 1:1 mixture of isopropanol and water was added to the test tube containing 50 mg of ZnS nanorod. The test tube was covered with rubber cap and nitrogen gas was purged from this mixture for 15 min, after gas purging the test tube was sealed with parafilm. This solution was then UV irradiated for 6 hours under continuous stirring. After the reaction, the test solution was filtered using cellulose filter. Then the test solution was analysed using UV-Vis spectrophotometer and HPLC.

4.5 Characterisation techniques

Optical absorption spectra were recorded with UV–Vis absorption spectrophotometer (Specord 205, Analytik Jena) and the room temperature photoluminescence studies were carried out by Fluorescence Spectrophotometer (Perkin Elmer LS55). For Absorption and emission studies, the nanostructures were dispersed finely in methanol using an ultrasonicator. To check the crystalline quality of the as-synthesized nanoparticles, X-ray diffraction of the nanostructures was carried out with the X-ray diffractometer (PANALYTICAL XPERT-PRO) using copper characteristic wave- length, 1.5418˚A and the scanning range is 20º-90º. The surface morphology, size and shape analysis of the nanostructures were done through scanning electron microscopy (JEOL JSM-6510LB) and TEM analysis (SAIF, IIT Bombay) was done using PHILIPS TEM analyser (Model: CM200) whose operating voltages and resolution are 20-200 kV and 2.4, respectively. For TEM, a drop of finely dispersed particles in spectroscopic grade methanol, was applied to carbon coated copper grid and then dried. Specific surface area was determined by nitrogen adsorption method by using smartsorb 91/92 instrument at 150ºC of regeneration of samples for one hour.

The photocatalysed reaction samples were analysed using UV-Vis spectrophotometer and high performance liquid chromatography (HPLC) (Agilent technologies). The chromatographic conditions: column, (C-18 column); mobile phase, methanol: water = 50:50 with a flow rate 1mL/min; UV detector at 254 nm for benzaldehyde reduction analysis; injection volume, 20 μL; column temperature, 25 ° C.

5. Results and discussion

Figure 4 shows the characteristic colours of as-synthesised ZnS nanospheres, nanorods and photodeposited samples.

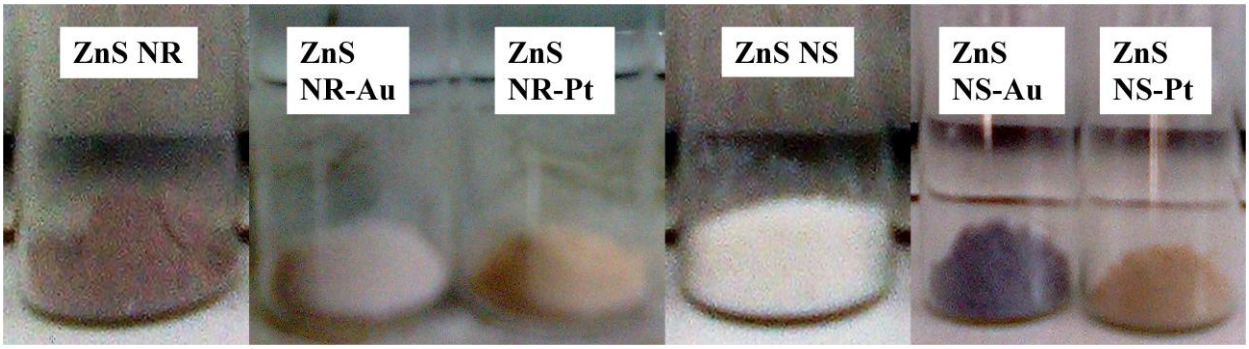

Figure 4. Various colours of as-synthesised ZnS nanostructures of different morphology.

Figure 5 shows the colours of the above samples after they were sintered at 500ºC due to improvement of crystallinity [41].

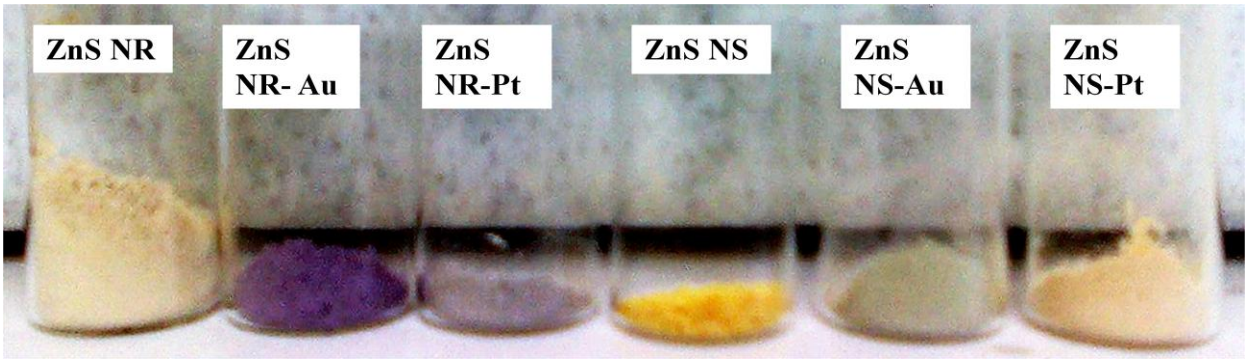

Figure 5. Various colours of as-synthesised ZnS nanostructures after thermal treatment at 500ºC for 2 h.

5.1 Absorption spectra

Figure 6 shows the UV-Vis absorption spectra of as-synthesised ZnS nanoparticles of different shapes.

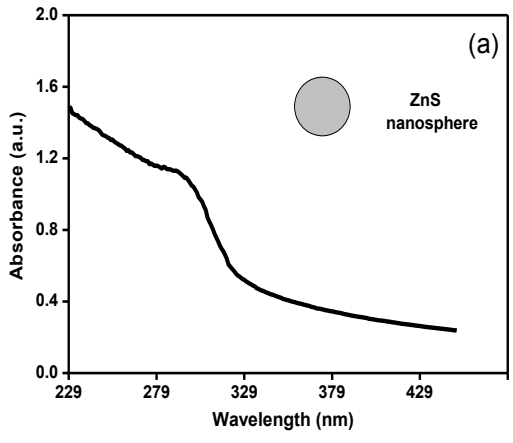

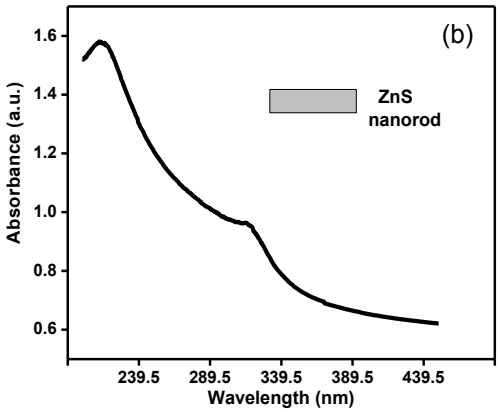

Figure 6. Absorption spectra of (a) ZnS nanospheres (b) ZnS nanorods.

It is evident from the Figure 6 that ZnS NS exhibit a strong absorption at wavelength 293 nm and ZnS NR at 316 nm. This suggests blue shift from the absorption edge of the bulk ZnS (336 nm) arising from quantum confinement effect in the nanoparticles [42]. The band gap of bulk ZnS is 3.68 eV at 300K. The band gap energy of the samples is calculated from the optical absorption experiment. The absorption coefficient α is determined from the transmittance data. The band gap for the as-synthesized nanoparticles has been evaluated from Tauc relation,

$$\alpha = A\,(h\upsilon - E\mathrm{g})^{n}/\,h\upsilon,$$

where A is a constant and Eg is the band gap of the material. Exponent n depends on the type of the transition; n may have values 1/2, 2, 3/2 and 3 corresponding to the allowed direct, allowed indirect, forbidden direct and forbidden indirect transitions respectively. The exact value of the band gap is determined by extrapolating the straight line portion of $(\alpha h\upsilon)^2$ vs. $h\upsilon$ graph to the $h\upsilon$ axis [43]. It was noticed that the band gap value for both ZnS nanospheres (3.95 eV) and nanorods (4.8 eV) is higher than the bulk value of ZnS (Figure 7).

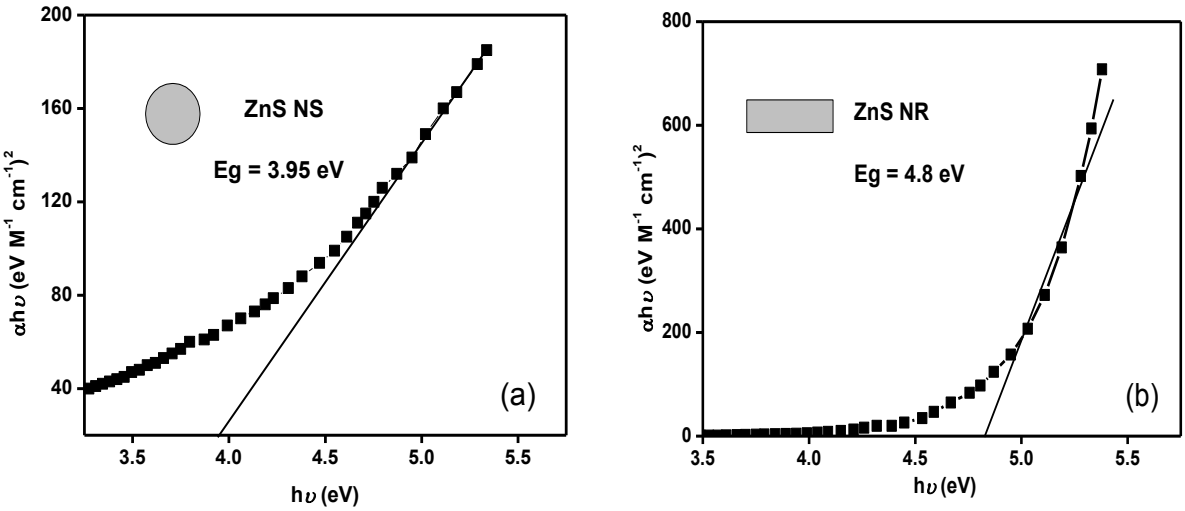

Figure 7. Tauc plot for the determination of the band gap of (a) ZnS nanospheres and (b) ZnS nanorods.

5.2 Photoluminescence spectra

The photoluminescence spectra of ZnS NS and photodeposited NS were recorded at room temperature with 320 nm excitation. A strong emission peak at 640 nm is observed in all the cases. A decrease in intensity of emission, i.e., quenching of photoluminescence is observed in photodeposited samples with maximum quenching taking place in case of platinum deposition (Figure 8a). This is attributed to the fact that with metal loading, the probability of recombination of electron-hole pair is reduced. The photoluminescence spectrum of ZnS NR and photodeposited NR was recorded with 290 nm excitation. The spectrum shows a strong emission peak at 580 nm associated with structural defects. Similar effect of metal loading was observed in photodeposited NR as in photodeposited NS (Figure 8b). Large amounts of surface defects at the interface of nanoparticles generate additional energy levels in the band gap. The e-h recombination at these centers leads to the emission in the ZnS nanoparticles [29, 44].

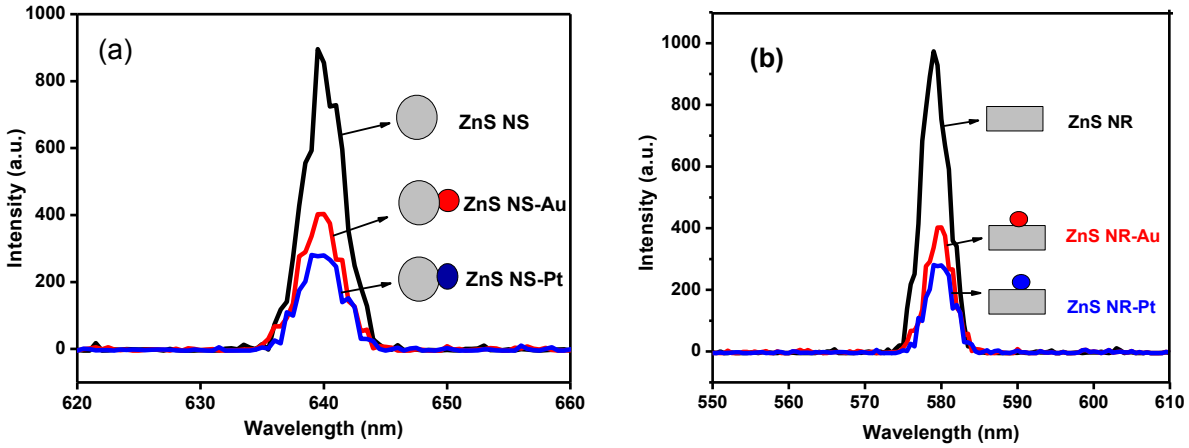

Figure 8. Photoluminescence spectra of (a) bare and 1 wt % Au & Pt deposited ZnS nanospheres (b) bare and 1 wt % Au & Pt deposited ZnS nanorods.

5.3 X-Ray diffraction patterns

Figure 9 shows the XRD patterns for as-prepared ZnS nanoparticles of different shapes.

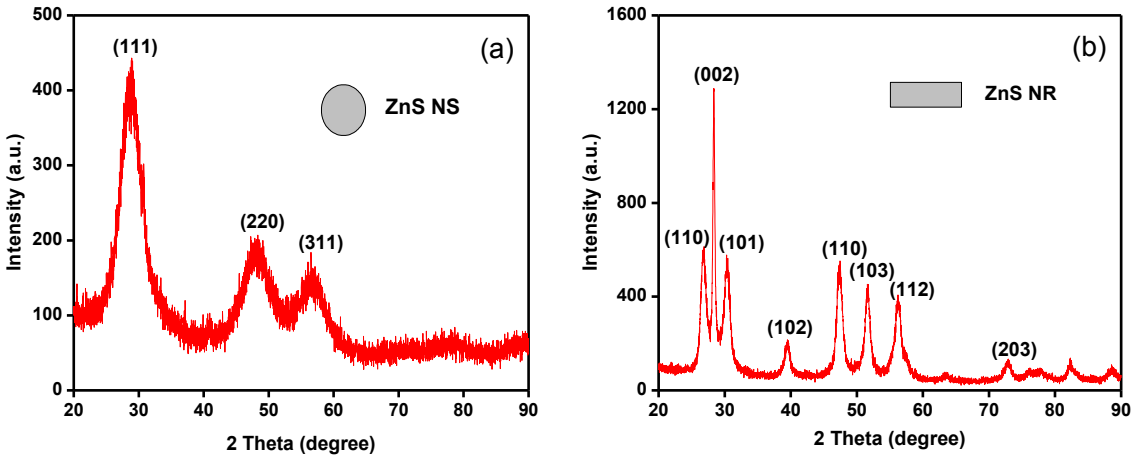

Figure 9. X-ray diffraction pattern of (a) ZnS nanospheres and (b) ZnS nanorods.

The XRD pattern of Figure 9a shows three diffraction peaks with 2Θ values of 29.09º, 48.1º and 57.88º. These peaks correspond to the (111), (220) and (311) planes of cubic zinc sulphide. From the XRD analysis, no characteristic peaks of impurity phases were observed. The calculated lattice constant, a = 5.041 A° is close to the reported value for cubic ZnS (JCPDS card No. 79–0043, a = 5.318 A°). The typical broadening of the peaks indicates that the size of the ZnS particles is very small. The XRD pattern shown in Figure 9b reveals that the ZnS product is in the wurtzite structure as the pattern shows diffraction peaks positioned at 2Θ values of 26.81°, 28.36°, 30.37°, 39.51°, 47.33°, 51.65°, 56.24° and 72.82° which can be indexed to (110), (002), (101), (102), (110), (103), (112) and (203) planes of wurtzite zinc sulphide. The relative high intensity of the (002) peak compared with those of other peaks indicates a preferential growth direction of the (002) plane in the pure wurtzite structure of ZnS sample. The calculated lattice constants a = 3.01 A° and c = 6.28 A° agree with the reported data (JCPDS File No. 05-0566 and No. 75-1534).

5.4 Surface area measurements

The Brunauer, Emmett and Teller (BET) adsorption-desorption of nitrogen gas was carried out to determine the surface area of nanoparticles. The surface area of ZnS NS is found to be 173.14 m^2/g. This high surface area suggests that the nanospheres are probably hollow

nanosphere because Hua-Feng et al. have reported synthesis of ZnS NS with a surface area of 97 m^2/g [28]. The surface area of NR was found to be 58.9 m^2/g. Some researchers have reported synthesis of ZnS NR having a surface area of 51m^2/g [45].

5.5 Scanning Electron Microscopy (SEM) analysis

Figure 10a & b shows the SEM images of ZnS nanoparticles prepared under the alkaline medium. The particles are spherical having diameter in the range of 2-5 µm. Their size can be controlled by reducing the temperature and time of refluxing because nanocrystal (NC) size increases with increasing reaction time as more material is added to NC surfaces and also with increasing temperature as the rate of addition of material to the existing nuclei increases [46]. The particles are agglomerated to form larger particles. This tendency to form cluters is due to the high surface energy of smaller particles. The high surface area (173.14 m^2/g) suggests that the nanospheres are hollow as compared to solid spheres of low surface area, 97 m^2/g as reported by Hua-Feng et al. Figure 10c shows the area from which EDS analysis has been done. Figure 10d shows a representative EDS spectrum of ZnS NS where Zn and S peaks can be clearly observed in this spectrum. Table 1 shows the calculated surface area, size and surface area to volume ratio of the particles.

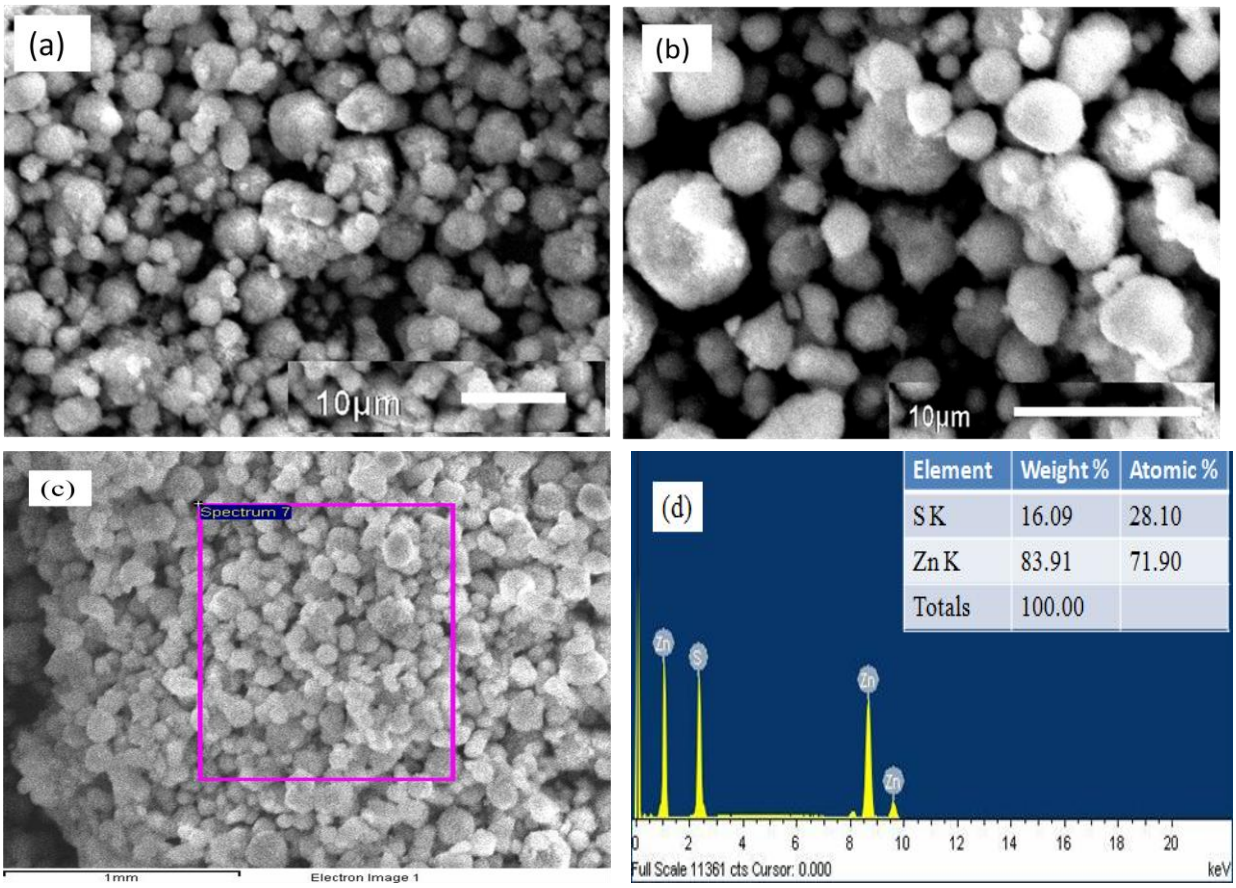

Figure 10. SEM images and EDS analysis of ZnS NS.

Table 1. Surface/Volume Ratio for ZnS nanospheres

S.no.	**Diameter (µm)**	**Radius (µm)**	**Surface area (S) (µm)^2**	**Volume (V) (µm)^3**	**S/V Ratio**
1.	3.75	1.87	44.19	27.62	1.60
2.	5.00	2.50	78.56	65.47	1.20
3.	4.37	2.18	60.01	43.71	1.37
4.	2.50	1.25	19.64	8.18	2.40
5.	3.12	1.56	30.59	15.91	1.92
6.	3.63	1.81	41.41	25.05	1.65
7.	2.64	1.32	21.90	9.63	2.27
8.	2.31	1.15	16.76	6.45	2.59
9.	2.97	1.48	27.72	13.72	2.02
10.	2.65	1.32	22.07	9.74	2.26
Average	3.29	1.64	36.28	22.55	1.93

The high surface to volume ratio which gradually decreases with particle size indicates the exhibition of nanosize property while showing particle size in micro-region (Figure 11).

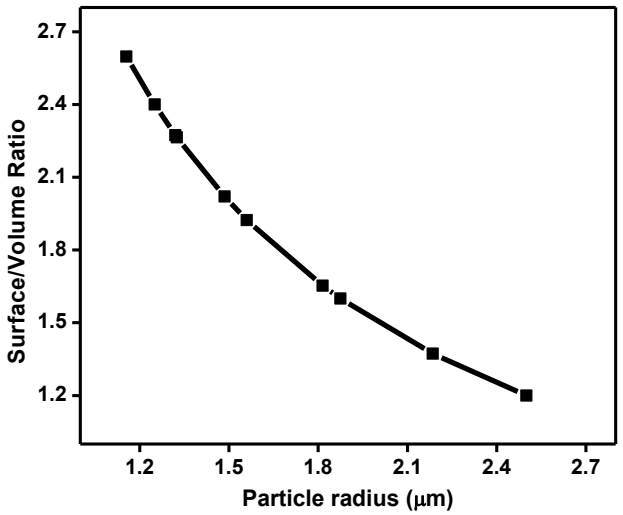

Figure 11. Surface/volume ratio as a function of the particle size.

Figure 12a-d shows the SEM images of as-synthesized ZnS NR. Figure 12e shows the area from which EDS analysis has been done. Figure 12f shows a representative EDS spectrum of a central part of a rod. Zinc and sulfur peaks are clearly seen in this spectrum. The Cu and C peaks in the EDS spectrum arise from the copper TEM grid used in the measurements. Table 2 shows the calculated surface area, size and surface to volume ratio for nanorods.

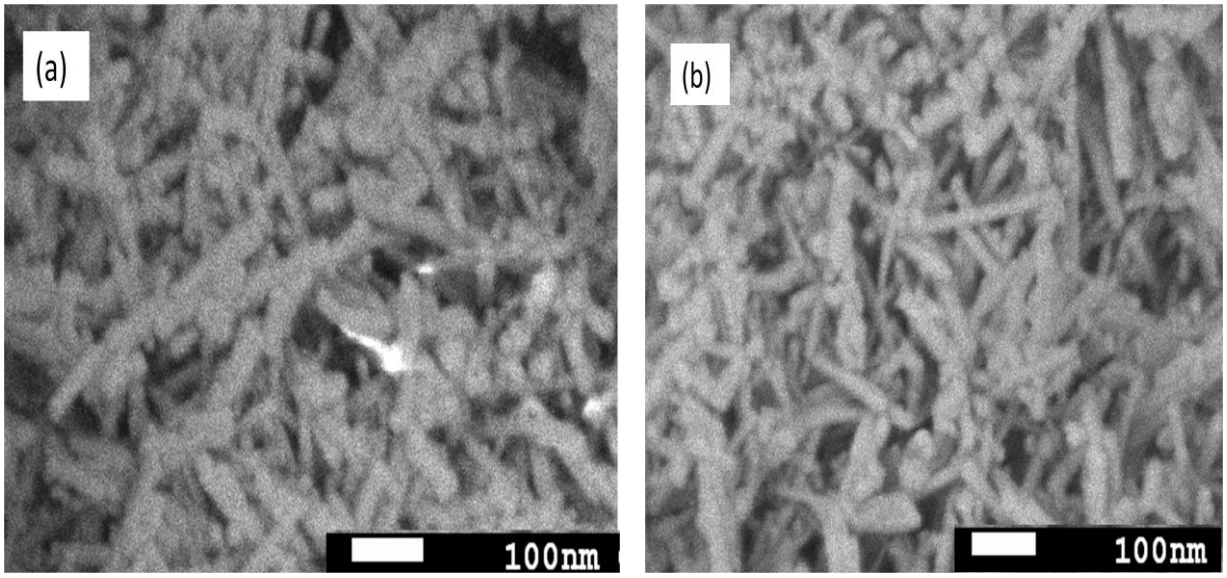

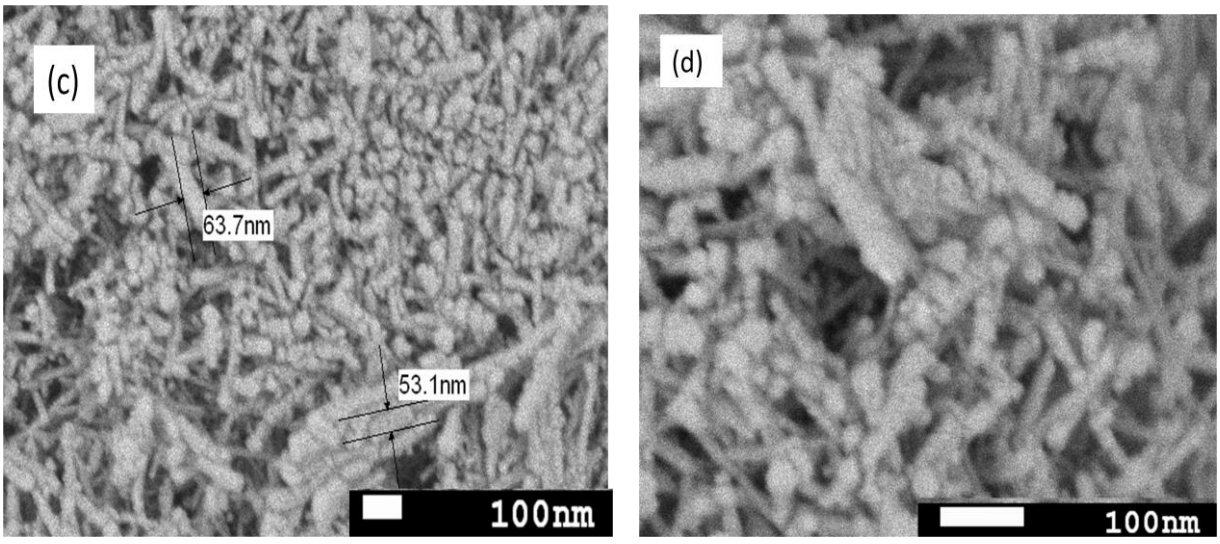

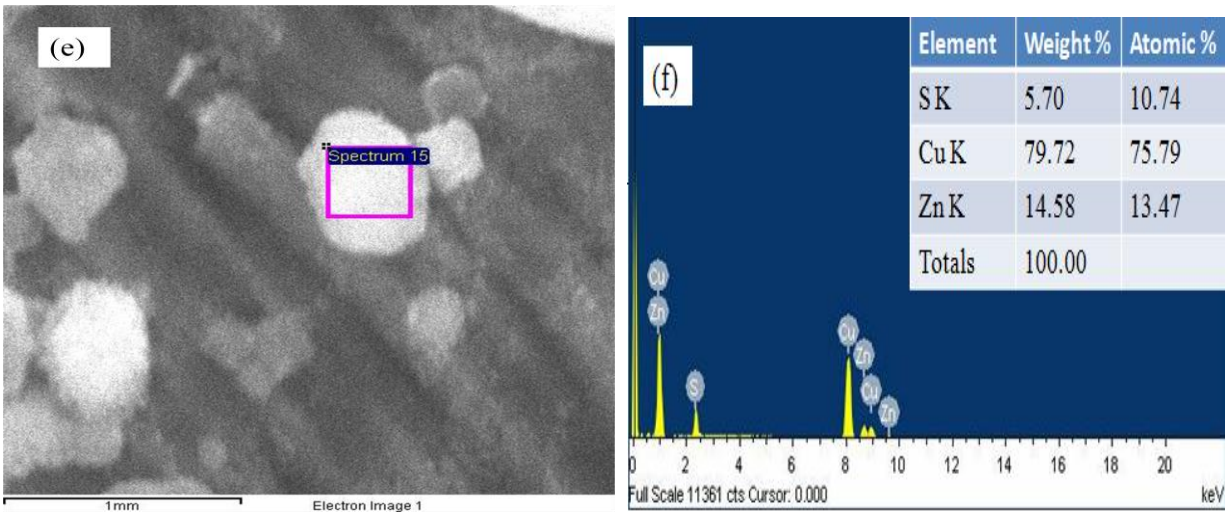

Figure 12. (a-d) SEM images of ZnS nanorods (e) SEM image showing the area selected for EDS analysis (f) EDS analysis of ZnS NR

5.6 Transmission Electron Microscopy (TEM) analysis

TEM images (Figure 13) of ZnS nanoparticles synthesised using solvothermal method shows that the product contains nanorods having diameter in the range of 10-20 nm and length varying between 50-120 nm. Several such images showed the monodisperse nanorods of aspect ratio = 3.3- 5.

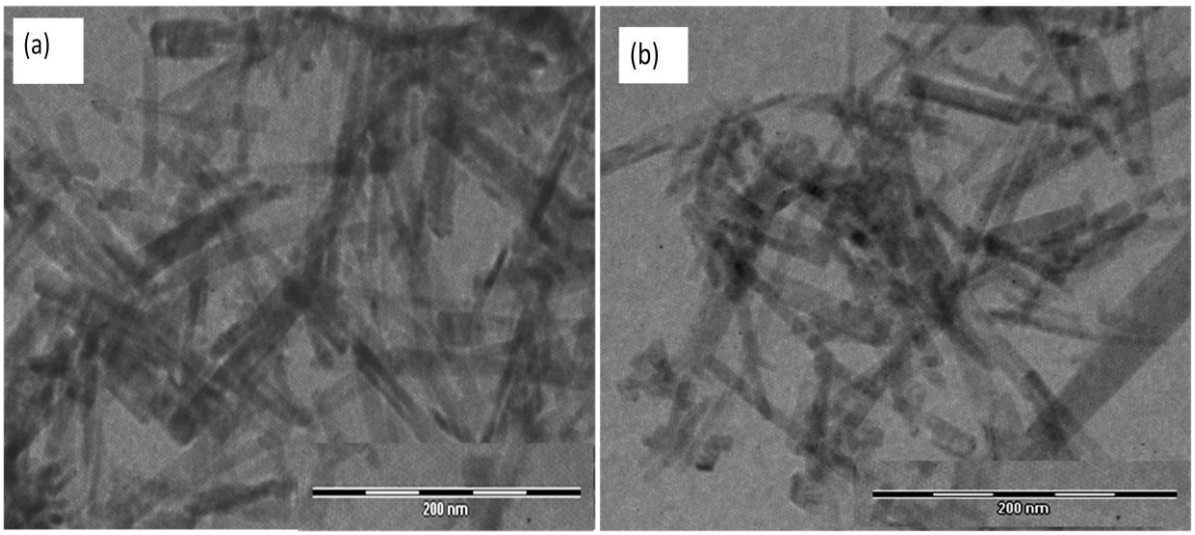

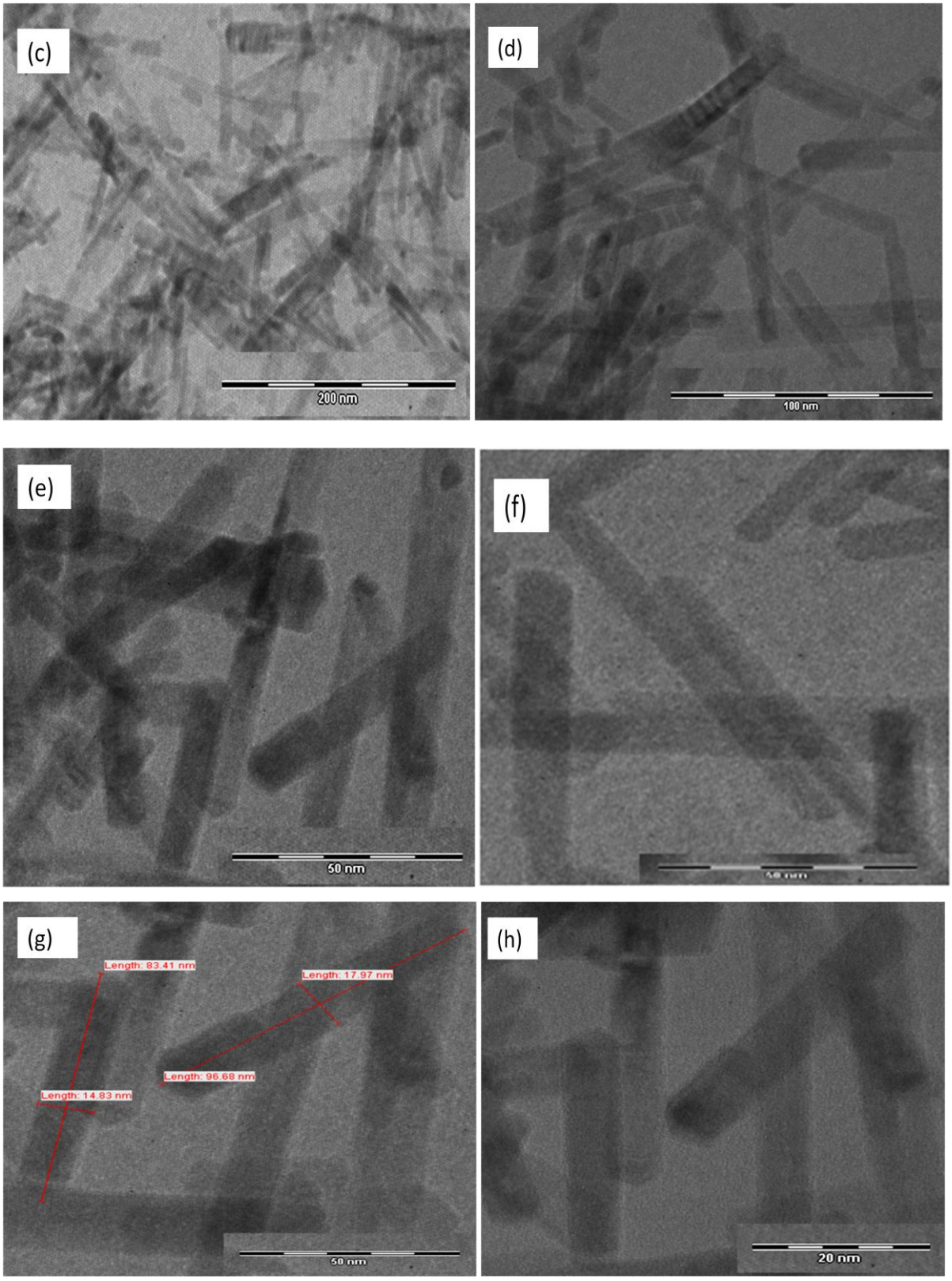
(c)
200 nm
(d)
100 nm
(e)
50 nm
(f)
(g)
Length: 83.41 nm
Length: 17.97 nm
Length: 96.68 nm
Length: 14.83 nm
50 nm
(h)
20 nm

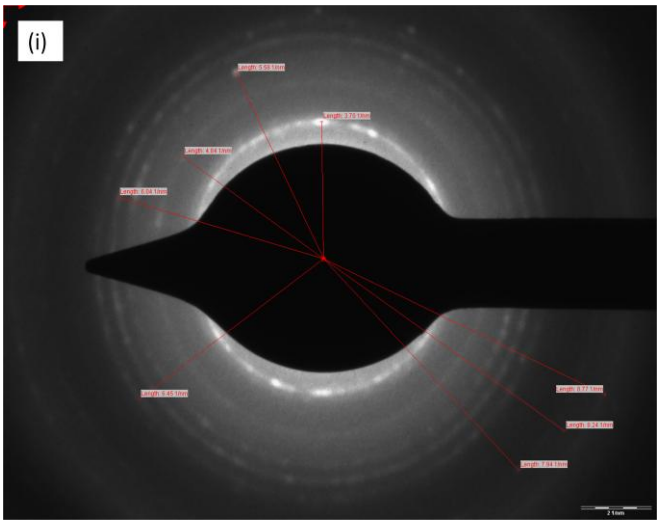

Figure 13. (a-h) TEM images of ZnS NR, (i) ED pattern for ZnS NR.

Table 2. Surface to volume ratio for ZnS nanorods

S. no.	**Diameter (nm)**	**Radius (nm)**	**Length (nm)**	**Surface area (S) (nm^2)**	**Volume (V) (nm^3)**	**S/V ratio**
1.	14.83	7.41	60.32	3154.16	10413.9	0.30
2.	17.97	8.98	64.48	4145.32	16345.22	0.25
3.	16.48	8.24	58.24	3440.15	12416.68	0.27
4.	13.8	6.9	59.28	2867.71	8862.08	0.32
5.	19.11	9.55	54.08	3818.44	15503.43	0.24
6.	17.54	8.77	55.12	3518.78	13311.84	0.26
7.	16.24	8.12	50.96	3012.70	10550.45	0.28
8.	15.93	7.96	80.95	4447.54	16125.68	0.27
9.	15.27	7.63	104.76	5389.09	19175.35	0.28
10.	12.82	6.41	106.1	4529.06	13688.66	0.33
Average	15.99	7.99	69.42	3832.29	13639.33	0.28

Table 1 and 2 shows NS have higher S/V ratio in comparison to NR. Though high S/V ratio is associated with high photocatalytic activity as more number of reactant molecules can adsorb to the surface, but this is not always the case. This can be explained on the basis that the NR exhibit a lower electron-hole recombination rate than the NS because of the greater charge mobility in the NR, which is enabled along the longitudinal dimension of the crystals and fewer localized states near the band edges and in the band gap due to fewer unpassivated surface states in the NR. Thus NS, in spite of having greater surface area, have lower activity than NR because of the greater electron-hole pair recombination probability.

Comparative physical properties of ZnS nanosphere and nanorod are presented in the Table 3.

Table 3. Physical properties of ZnS-NS and NR

	Absorption onset	**Band gap**	**Fluorescence emission**	**Crystal phase**	**Characterstic Size**	**Surface area**
ZnS NS	320 nm	3.95 eV	640 nm (*320 nm)	Cubic	Dia. = 2-5 µm	173.14 m^2/g
ZnS NR	338 nm	4.8 eV	580 nm (*290 nm)	Wurtzite	Aspect ratio = 3.3-5	59 m^2/g
Pt-ZnS NR	338 nm	4.8 eV	580 nm (with decreased intensity compared to NR) (*290 nm)	Wurtzite	-	61 m^2/g

*Excitation wavelength

5.7 Results of the photocatalytic reactions

Photocatalytic degradation of p-nitrophenol

Figure 14 depicts the time course of degradation of 5 mL of 10 µM PNP solution after 4 hour reaction with ZnS NR, photodeposited ZnS NR and sintered NR. The band between 380-420 nm, which arises from the starting compound decreases as the oxidation proceeds. A slight increase in the absorbance of the band between 290-335 nm is seen. As can be noticed, the extent of photocatalytic degradation of PNP by ZnS-NR after metal deposition and sintering is significantly improved. Pt loaded ZnS particles showed higher photoactivity as compared to Au-ZnS composites.

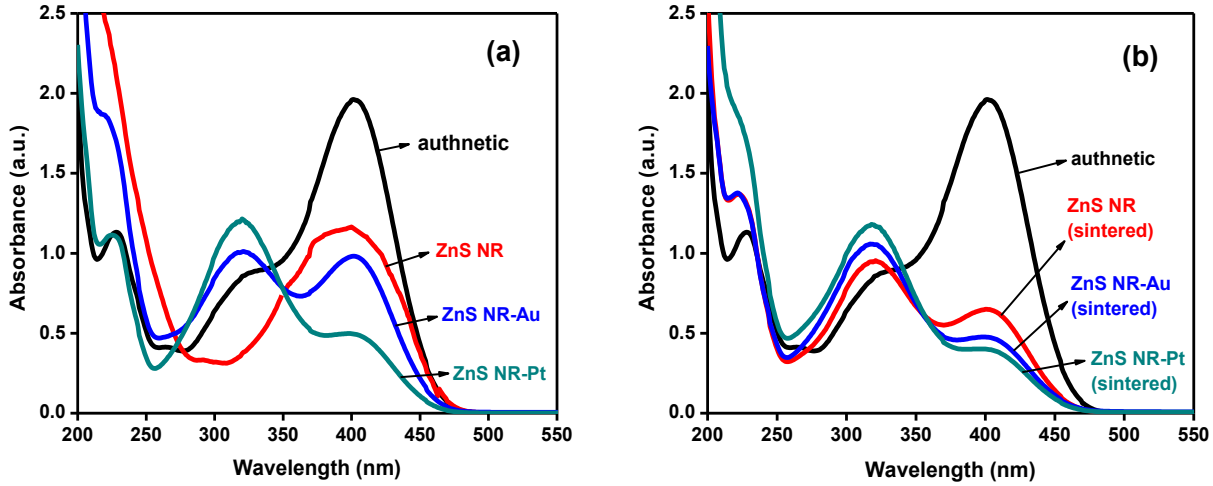

Figure 14. UV-Vis spectra of p-nitrophenol solution degraded by (a) as-synthesized ZnS-NR and (b) sintered ZnS-NR after 4 h light irradiation.

Figure 15 shows the UV-Vis spectral changes during photocatalytic degradation of PNP by ZnS NS after 2 and 4 h irradiation and the effect of metal loading and thermal treatments. With increase in time of irradiation, the percentage of photodegradation increased. This is because of the fact that with increase in the time of irradiation, the number of photons absorbed (quantum flux) by the catalyst is more producing higher amount of $O^{2\bullet-}$ and $OH^{\bullet}$ radicals. As a result of which more amount of PNP is absorbed by the catalyst. Similar effects of metal loading and sintering were observed in case of nanospheres as in nanorods.

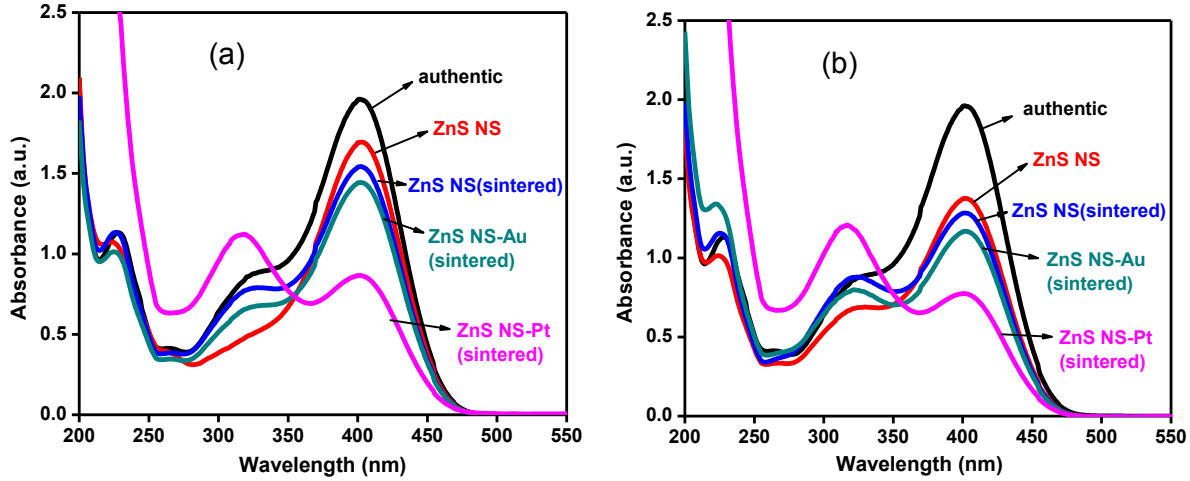

Figure 15. UV-Vis spectra of PNP photodegradation after (a) 2 h and (b) 4 h irradiation.

The comparative rates of photocatalytic degradation by various ZnS nanostructures are shown below.

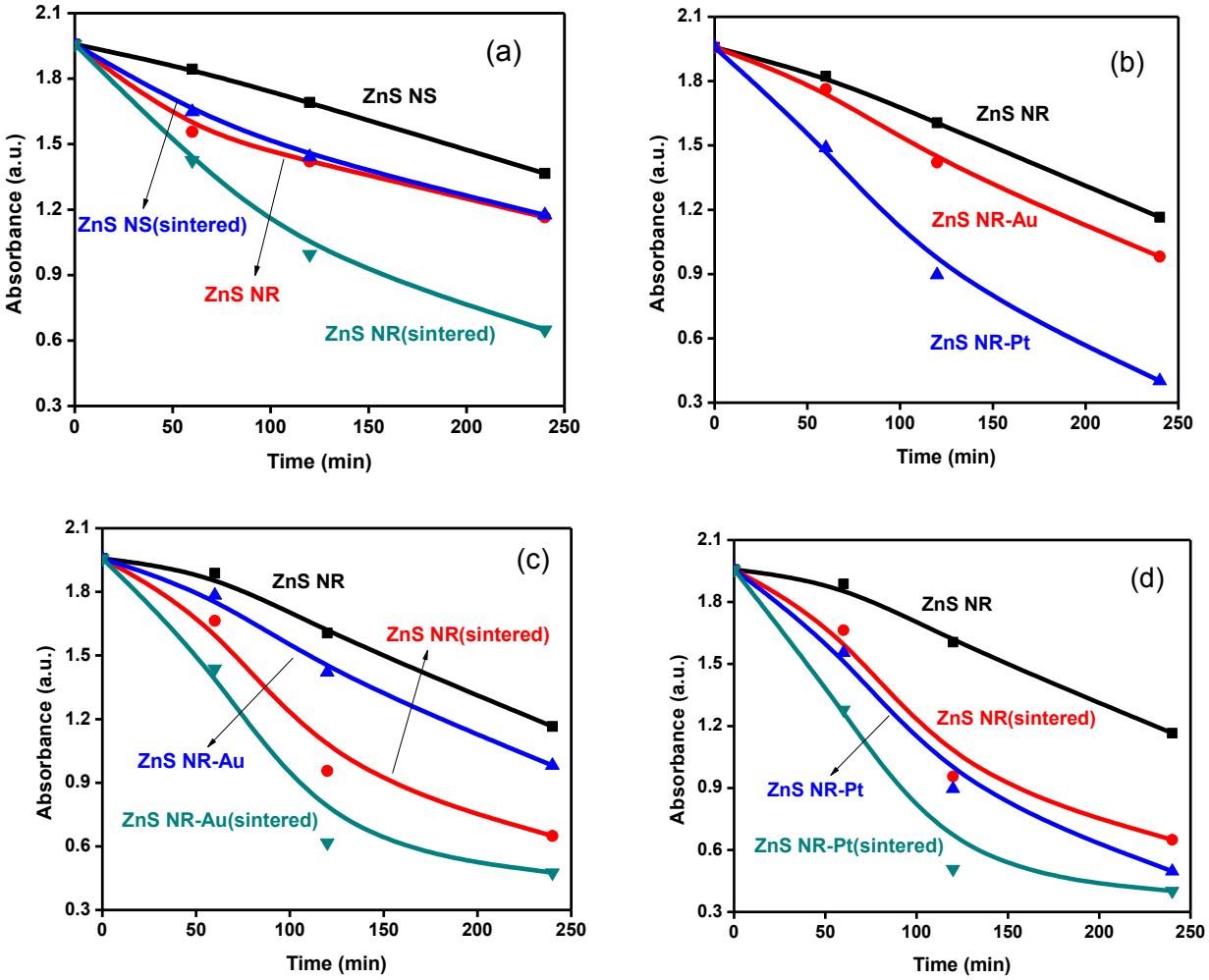

Figure 16. Comparative photocatalytic activity of (a) nanospheres and nanorods (b) bare, Au and Pt deposited nanorods and (c, d) sintered and non-sintered nanorods.

Degradation rates were found to be lower for NS as compared to NR (Figure 16a). This is because of the higher photon absorption cross-section and reduced recombination probability that results in higher activity of nanorods. With bare ZnS nanorods, the decrease in absorbance is not significant. However, with metal loading, the degradation rate is enhanced which can be explained as follows. When the noble metal is loaded onto the surface of the photocatalyst, the photogenerated electrons migrate to the surface of the host photocatalyst and are entrapped by the noble metal cocatalyst. Meanwhile, the photogenerated holes stay at the host photocatalyst and migrate to its surface. This results in the efficient separation of the photogenerated electrons and holes. Subsequently, the separately localized electrons and holes become involved in their roles as the reducer and oxidizer, respectively, in the photocatalytic reaction. The rate of degradation in case of Pt deposition is more than that of Au loading (Figure 16b).

Degradation rates were found to be greatly increased in case of sintered catalysts (Figure 16c & d). This higher photocatalytic activity of sintered catalysts can be explained on the basis that with sintering, the internal lattice defects and surface defects of ZnS, which act as photocarrier trap during the transfer process of charge carriers, are popped out due to growth of ordered crystalline phases.

Photocatalytic oxidation of Benzaldehyde

Figure 17a shows the UV-Vis spectral changes of benzaldehyde solution after reaction with ZnS NR and Au-ZnS NR under different intervals of light irradiation. Higher activity is observed with photodeposited nanorods as compared to bare sample. This is attributed to the improved charge transfer process. Also, with increase in time of irradiation, percentage of oxidation is increased which can be explained on similar grounds as in case of p-nitrophenol degradation. Figure 17b shows the absorbance vs time graph for benzaldehyde oxidation by bare and Au deposited ZnS NR.

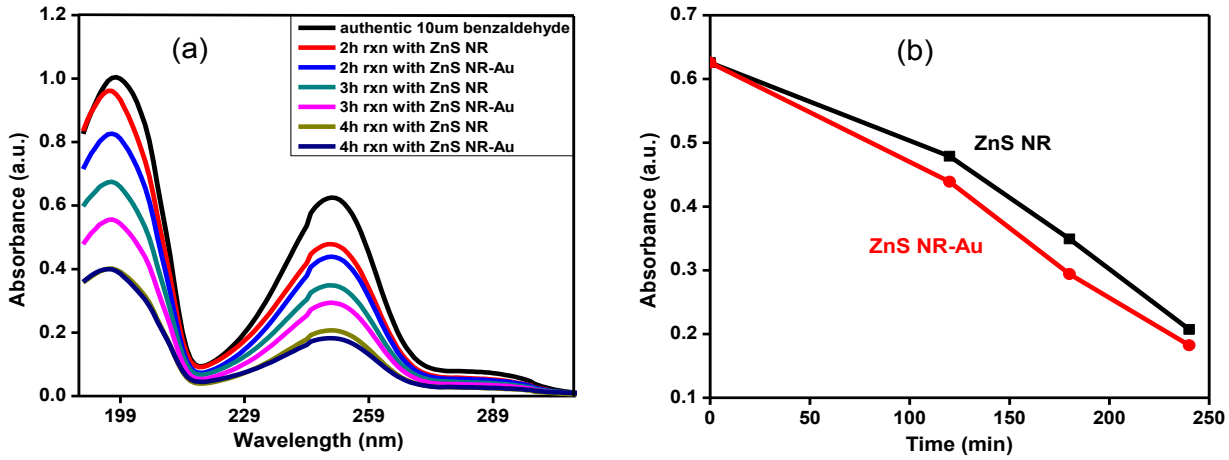

Figure 17. (a) UV-Vis spectra for benzaldehyde solution degraded under different time intervals (b) Absorbance vs Time graph to show the effect of metal loading.

Photocatalytic reduction of Benzaldehyde

The reduction ability of ZnS was analysed by its reaction with benzaldehyde. The reduction potential of benzaldehyde is approx. –0.80 eV, considerably lower than that of ZnS (-1.85 eV) and hence it can be reduced by ZnS. The reduced samples were analysed by UV-Vis and HPLC techniques. Figure 18 and 19 show the UV-Vis spectra and HPLC chromatogram for benzaldehyde reduction. Though no clear changes are visible from the UV-Vis spectra, the HPLC chromatogram shows the decrease in absorbance of benzaldehyde and appearance of new

peak at R_t = 2.1 min. This new peak may be attributed to benzyl alcohol although quantitive analysis is not done with the authentic sample of benzyl alcohol.

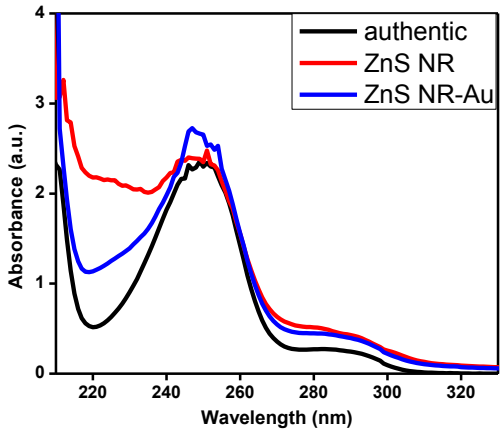

Figure 18. UV-Vis spectra for benzaldehyde reduction.

HPLC analysis :

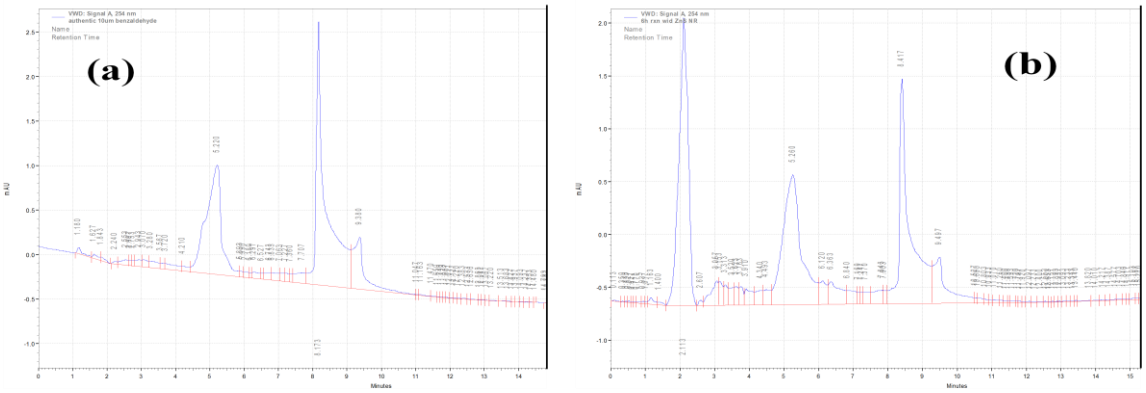

Figure 19. HPLC Chromatograms for reduction of benzaldehyde (a) authentic 10 µM benzaldehyde (b) after 6 h rxn with ZnS NR.

The following table shows the data obtainted from HPLC analysis:

	Concentration of Benzaldehyde (µmole)
Authentic	0.0500
After 6h rxn with ZnS NR	0.0206
After 6h rxn with ZnS NR-Au	0.0140

6. Conclusions

In summary, ZnS nanospheres and nanorods were successfully fabricated and characterized by their absorption spectra, photoluminescence spectra, X-Ray diffraction patterns, SEM and TEM images. The as-synthesised nanospheres and nanorods have a band gap of 3.95 eV and 4.8 eV resp. XRD patterns showed that NS have zinc blende structure while the NR are in wurtzite phase. The spherical particles were found to have diameter in the range of 2-5 μm as calculated from their SEM images. The nanorods are 50-110 nm long and have a diameter of 15-20 nm and aspect ratio 3.3-5. The photocatalytic efficiency of ZnS was checked by reaction with p-nitrophenol and benzaldehyde. PNP degradation studies revealed that nanorods exhibit higher catalytic activity as compared to nanospheres. Also, the efficiency of degradation was found to be significantly enhanced with metal loading, with platinum giving higher rates. Thermal treatment of ZnS structure always exhibits improved photoactivity due to growth of more crystalline phases. Higher rates of oxidation with photodeposited NR in comparison to bare NR were also observed in benzaldehyde oxidation. Reduction of benzaldehyde was carried out in order to analyse the reducing ability of ZnS. Due to the highest reduction ability/ H_2 photoproduction efficiency, it is expected that ZnS may show the superior reductive ability compared with mostly used photocatalysts. However, this could aspect not be shown because of shortage of time.

7. References

1. Chen, X.; Samuel S.; Mao, S. *Chem. Rev*. **2007**, *107*, 2891-2959.
2. Hoffmann, M. R.; Martin, S. T.; Choi, W.; Bahnemann, D.W.; *Chem.Rev.* **1995**, *95*, 69-96.
3. Mills, A.; Hunte, S. Le. *J. Photochem. Photobiol. A: Chem.* **1997**, *108*, 1-35.
4. Palmisano, G.; Augugliaro, V.; Pagliaro, M.; Palmisano, L. *Chem. Commun.* **2007**, 3425–3437.
5. Fox, M.A.; Dulay, M. *Chem. Rev.* **1995**, *83*, 341357.
6. Bellardita, M.; Addamo, M.; Paola, A.D.; Palmisano, L. *Chem. Phys*., **2007**, *339*, 94–103.
7. Wang, S.; Wang, T.; Chen, W.; Hori, T. *Chem. Commun.*, **2008**, 3756–3758.
8. Kamat P.V.; Meisel D. *Current Opinion in Colloid & Interface Science* **2002**, *7*, 282-287.
9. Shon, H.; Phuntsho, S.; Okour, Y.; Cho, D.L.; Kim, K.S.; Li, H.J.; Na, S.; Kim, J.B.; Kim, J.H. *J. Korean Ind. Eng. Chem.* **2008**, *19*, 1-16
10. Anpo, M. *Pure Appl. Chem.* **2000**, *72*, 1265–1270.
11. Beecroft, L.L.; Ober, C.K. *Chem. Mater.* **1997,** *9*, 1302-1317.
12. Alivisatos, P. *J. Phys. Chem*. **1996**, *100*, 13226-13239.
13. Hagfeldtt; Gratzel, M. *Chem. Rev.* **1995**, *95*, 49-68.
14. Kudo, A.; Miseki, Y. *Chem. Soc. Rev*. **2009**, *38*, 253–278.
15. Thiruvenkatachari, R.; Vigneswaran, S.; Moon, S. *Korean J. Chem. Eng*. **2008**, *25*, 64-72.
16. Linsebigler, A.L.; Lu, G.; Yates, J.T. Jr. *Chem. Rev.* **1995**, *95*, 735-758.
17. Htoon, H.; Hollingsworth, J.A.; Malko, A.V.; Dickerson, R.; Klimov, V.I. *Appl. Phys. Lett.* **2003**, *82*, 4776–4778.
18. Thomas, K.G.; Barazzouk, S.; Ipe, B.I.; Joseph, S.T.S.; Kamat, P.V. *J. Phys. Chem. B*, **2004**, *108*, 13066-13068.
19. Huang, F.; Banfield, J.F. *J. Am. Chem. Soc.* **2005**, *127*, 4523-4529.
20. Mclaren, A.; Solis, T.V.; Li, G.; Tsang, S.C. *J. Am. Chem. Soc.* **2009**, *131*, 12540–12541.
21. Wu, N.; Wang, J.; Tafen, D.N.; Wang, H.; Zheng, J.G.; Lewis, J.P.; Liu, X.; Leonard, S.S.; Manivannan, A. *J. Am. Chem. Soc.* **2010**, *132*, 6679–6685.
22. Chen, X.; Shen, S.; Guo, L.; Mao, S.S. *Chem. Rev.* **2010**, *110*, 6503–6570.
23. Wang, S.; Wang, T.; Chen, W.; Hori, T. *Chem. Commun.*, **2008**, 3756–3758.
24. Pal, B.; Ikeda, S.; Kominami, H.; Kera, Y.; Ohtani, B. *Journal of Catalysis* **2003**, *217*, 152–159.
25. Wang, H.; Partch, R.E.; Li, Y. *J. Org. Chem.* **1997,** *62*, 5222-5225.
26. Saravanan, N.; Teh, G.B.; Yap, S.Y.P.; Cheong, K.M. *J Mater Sci: Mater Electron* **2008**, *19*, 1206–1208.

27. Bredol, M.; Kaczmarek, M. *J. Phys. Chem. A* **2010**, *114*, 3950–3955.
28. Shao, H.F.; Qian, X.F.; Zhu, Z.K. *Journal of Solid State Chemistry* **2005**, *178*, 3522–3528.
29. Li, Z.; Liu, B.; Li, X.; Yu, S.; Wang, L.; Hou, Y.; Zou, Y.; Yao, M., Li, Q.; Zou, B.; Cui, T.; Zou, G.; Wang, G.; Liu, Y. *Nanotechnology* **2007,** *18***,** 255602 (7pp).
30. Lan, C.; Hong, K.; Wang, W.; Wang, G. *Solid State Communications* **2003**,*125*, 455–458.
31. Zhou, G.T.; Wang, X.; Yu, J.C. *Crystal Growth & Design*, **2005**, *5*, 1761-1765.
32. Arai, T.; Senda, S.; Sato, Y.; Takahashi, H.; Shinoda, K.; Jeyadevan, B.; Tohji, K. *Chem. Mater.* **2008**, *20*, 1997–2000.
33. Ranjit, K.T.; Krishnamoorthy, R.; Viswanathant, B. *Photochem Photobiol. A: Chem.* **1994**, *81*, 55-58.
34. Yin, H.; Wada, Y.; Kitamura, T.; Yanagida, S. *Environ. Sci. Technol.* **2001**, *35*, 227-231.
35. Yanagida, S.; Ishimaru, Y.; Miyake, Y.; Shiragami, T.; Pac, C.; Hashimoto, K.; Sakata, T. *J. Phys. Chem.* **1989**, *93*, 2516-2582.
36. Liu, J.; Geng, B.; Wang, S. *Crystal Growth & Design* **2009**, *9*, 4384-4390.
37. Chen, X.; Xu, H.; Xu, N.; Zhao, F.; Lin, W.; Lin, G.; Fu, Y.; Huang, Z.; Wang, H.; Wu, M. *Inorganic Chemistry* **2003**, *42*, 3100-3106.
38. Jindal, Z.; Verma, N.K. *Physica E* **2011**, *43*, 1021–1025.
39. Kar, S.; Biswas, S.; Chaudhuri, S. *Synthesis and Reactivity in Inorganic, Metal-Organic and Nano-Metal Chemistry* **2006**, *36*, 193–196.
40. Datta, A.; Panda, S.K.; Chaudhuri, S. *J. Phys. Chem. C* **2007,** *111*, 17260-17264.
41. Park, K.; Yu. H.J.; Chung. W.K.; Kim, B.J.; Kim, S.H. *J Mater Sci* **2009**, *44*, 4315–4320.
42. Pradhan, N.; Efrima, S. *J. Phys. Chem. B* **2004,** *108*, 11964-11970.
43. Borah, J.P.; Barman, J.; Sarma, K.C. *Chalcogenide Letters* **2008,** *5*, 201- 208.
44. Pol, S.V.; Pol, V.G.; Calderon-Moreno, J.M.; Cheylan, S.; Gedanken, A. *Langmuir* **2008**, *24*, 10462-10466.
45. Xi, G.; Wang, C.; Wang, X.; Zhang, Q.; Xiao, H. *J. Phys. Chem. C* **2008**, *112*, 1946-1952.
46. Burda, C.; Chen, X.; Narayanan, R.; El-Sayed, M.A. *Chem. Rev.* **2005,** *105*, 1025-1102.